Broadband control of topological-spectral correlations in space-time beams

Marco Piccardo,[1, 2, 3, *] Michael de Oliveira,[1, 4] Veronica R. Policht,[4] Mattia Russo,[4] Benedetto Ardini,[4] Matteo Corti,[4] Gianluca Valentini,[4] Jorge Vieira,[2] Cristian Manzoni,[5] Giulio Cerullo,[4] and Antonio Ambrosio[1, †]

[1]*Center for Nano Science and Technology, Fondazione Istituto Italiano di Tecnologia, Milan, Italy*
[2]*Department of Physics, Instituto Superior Técnico,*
Universidade de Lisboa, 1049-001 Lisbon, Portugal
[3]*Instituto de Engenharia de Sistemas e Computadores – Microsistemas*
e Nanotecnologias (INESC MN), 1000-029 Lisbon, Portugal
[4]*Physics Department, Politecnico di Milano, Milan, Italy*
[5]*Institute for Photonics and Nanotechnology, Consiglio Nazionale delle Ricerche, Milan, Italy*

The synthesis of ultrashort pulses with simultaneously tailored spatial and temporal properties opens new horizons in multimode photonics, especially when the spatial degree of freedom is controlled by robust topological structures. Current methods to shape space-time beams with correlations between their topological charges and spectral components have yielded fascinating phenomena. However, shaping is currently limited to narrow topological and/or spectral bands, greatly constraining the breadth of achievable spatiotemporal dynamics. Here, we introduce a Fourier space-time shaper for ultra-broadband pulses, covering nearly 50% of the visible spectrum and carrying a wide range of topological charges with values up to 80. Instead of relying on a conventional grating with linear geometry, our approach employs a diffractive axicon with circular geometry that allows to impart azimuthal phase modulations to beams carrying orbital angular momentum. We retrieve the spatiotemporal field by introducing a characterization technique based on hyperspectral off-axis holography. The tailoring of linear topological-spectral correlations enables the control of several properties of the wave packets, including their chirality, orbital radius, and number of intertwined helices, while complex correlations allow us to manipulate their dynamics. Our space-time beams with broadband topological content will enable a host of novel applications in ultrafast light-matter excitations, microscopy, and multiplexing.

Space-time coupling in ultrashort optical pulses, such as pulse-front tilt and pulse-front curvature, generally occurs when the spatial properties of a broadband light beam are frequency-dependent [1]. These kinds of chromatic aberrations have been known for decades, but have often been regarded as undesirable distortions of the spatiotemporal pulse structure, and sometimes even ignored. Only more recently, with significant advances in wavefront [2] and pulse shaping [3], space-time wave packet engineering has begun to flourish [4, 5]. This is part of a broader trend toward highly multimode photonics [6–8], in which space-time beams represent one of the richest and most complex frontiers in terms of combinations of optical degrees of freedom.

The synthesis of space-time beams with nonseparable spatiotemporal states has led to spectacular demonstrations of localized wave packets with exotic refraction and controllable group velocity [9–11]. Among the many degrees of freedom exploited in complex spatiotemporal light, the topological charge of beams, ℓ, carrying orbital angular momentum (OAM) is the key component in many methods, including time-varying OAM beams [12, 13], spatiotemporal optical vortices with transverse OAM [14–16], light coils [17, 18], revolving-rotating beams [19], and toroidal pulses [20, 21]. Vortex beams, in particular, have been widely studied given that the constituting OAM modes benefit from a robust topological

structure, form a convenient basis for signal multiplexing [22], and are suitable for the excitation of topological light-matter interactions.

Most space-time beam shaping methods are based on a two—or more [11, 13, 23]—step process, in which a linear grating is used to angularly disperse the incoming pulse and a holographic device placed at the Fourier plane of the grating modulates the spatially-separated spectral components of the input pulse [5]. When these schemes are employed to define a correlation between the frequencies and topological charges of a pulsed beam, it becomes apparent that the linear geometry of the grating in conventional pulse shapers is mismatched to the circular symmetry of beams carrying orbital angular momentum. Due to this inherent limitation, all demonstrations of topological-spectral correlations thus far have resulted in pulses with a limited OAM bandwidth with values of topological charge around unity [11, 13, 18, 24] and, in most cases, in a relatively narrow band of optical frequencies, corresponding to pulse durations in the picosecond range.

Here we demonstrate a Fourier space-time shaper based on an axicon grating with circular geometry to map frequencies across nearly 140 THz (200 nm) of spectral bandwidth onto concentric radial rings to which we can impart azimuthal phase modulations with a wide content of OAM. We are able to generate separable

and nonseparable space-time beams with tailored linear and complex (beyond linear) topological-spectral correlations, which display unprecedented spatiotemporal dynamics. In demonstrating broadband operation we overcome many challenges in the achromatic modulation, Fourier transformation, aberration correction, recombination and spatiotemporal characterization of ultrashort wave packets, establishing a ready-to-use scheme to serve new applications in ultrafast science and technology.

Results

Broadband space-time shaper

The conceptual scheme for the synthesis of spatiotemporal light fields with broadband topological-spectral correlations is presented in Fig. 1c (for a detailed setup schematic see Fig. 2a). The coherent light source is a non-collinear optical parametric amplifier (NOPA) [25, 26] delivering broadband (530–700 nm) visible femtosecond pulses compressed to nearly transform-limited duration by a set of chirped dielectric mirrors [27] (Fig. 1a). The core element of our synthesizer is a multilevel axicon grating fabricated in house on fused silica by grayscale lithography (Fig. 1d), which has clear advantages in terms of efficiency and spectral shaping capabilities with respect to simpler binary gratings (Supplementary Note 1). The axicon design parameters—in particular, its period and size —are tuned to maximize the spectral resolution of the space-time synthesizer, allowing us to address around 40 independent spectral windows in the correlation function (Materials and Methods). Both this value and the large topological charges that can be achieved in our synthesizer are an order of magnitude larger than those achieved in previous systems [13, 18, 24], bringing unprecedented flexibility and control in the design of space-time beams carrying OAM.

We access the far field of the axicon using a spherical concave mirror (Fig. 2a), which carries out a broadband spatial Fourier transform. At the Fourier plane, the pulse is dispersed into concentric rings with wavelengths linearly distributed along the radial direction, as characterized by a hyperspectral camera [28] (Fig. 1b). The spectrally-dependent spatial structure of the space-time beam is defined by a spatial light modulator (SLM) imposing an arbitrary topological-spectral coupling in the Fourier plane of the axicon. The phase hologram displayed on the SLM is divided into a finite set of concentric rings, each assigning a single topological charge to a different spectral window of the ultrashort pulse (Fig. 1f). In addition to imparting the OAM content, the hologram also corrects for astigmatic aberrations of the system and for the wavelength-dependent phase response of the SLM, which is essential to account for when operating with a broadband spectrum (Supplementary Note 2).

After the beam shaping using the SLM, the beam is inversely Fourier transformed by a concave mirror (Fig. 2a). At the image plane of the axicon we obtain a novel family of high-order Bessel beams with a tailored topological-spectral correlation. In principle, by passing through a conjugate grating and propagating further to the far field we could convert these to a family of Laguerre-Gaussian modes (Extended Data Fig. 6), as this would cancel out the axicon's phase contribution to the beam, which is responsible for the Bessel component. We choose, however, to avoid the second grating and keep the Bessel profiles as they provide some important advantages over the Laguerre-Gaussian ones: first, they mitigate both OAM- and frequency-dependent diffraction (Supplementary Note 3), which would be detrimental to the spatiotemporal dynamics upon beam propagation [4], and second, they benefit from self-healing [29], making the beam robust against possible obstructions or turbulence over its path.

On-axis holography

We first validate our setup with the synthesis of a pulsed vortex beam, a separable space-time beam in which all frequencies have the same topological charge, here with a value of $\ell = 40$ (Fig. 1e). The structured beam is characterized by on-axis holography, interfering it with a collinear reference beam with variable delay (Fig. S3e). Subtracting the non-interfering intensity components of the structured and reference beams from the camera image, we obtain a profile directly proportional to the real part of the electric field of the ultrashort pulse [30]. The retrieved profile reveals the spatiotemporal separability, showing a doughnut-like profile that only exhibits a change in amplitude without any spatial dependence as a function of delay (Fig. 1g). The axicon grating-based method presented here outperforms previous schemes for achromatic vortex generation of ultrashort pulses [31–35], ranging from dispersion compensation and geometric phase accumulation to conical glasses based on total internal reflection, both in terms of beam quality and magnitude of the encoded topological charge.

Next, we generate a nonseparable space-time beam in which the topological charge scales linearly with frequency, ranging from $\ell = 30$ to 50 over the spectral bandwidth (Fig. 1f). The correlation is discretized in steps $\delta\ell = 1$ rather than being a continuous curve, to avoid noninteger values corresponding to beams with fractional OAM, which may not be invariant over their propagation and suffer from distortion [36]. Our method allows us to synthesize a helical wave packet [5, 37], originally introduced as a "light spring" [17], with a rotating envelope as shown by on-axis holography (Fig. 1h). The rotation results from a spatially-dependent delay of the pulse arrival time, which varies along the azimuthal coordinate [17]. This wave packet describes a coil structure in space, which essentially translates rigidly in the z direction as it propagates (Extended Data Fig. 1).

Hyperspectral off-axis holography

While on-axis holography provides a partial character-

ization of the structured beam, it does not allow a full reconstruction of its complex electric field. This limitation can be circumvented by introducing a small angle between the structured and reference beams. This technique, known as off-axis digital holography [38], can provide both the amplitude and phase of the field, with respect to that of the reference, by filtering one of two first order terms from the spatial Fourier transform of the interference pattern. By scanning the time delay between the structured and reference beams, the full complex electric field, $E(x,y,t)$, can be reconstructed. Though off-axis digital holography has been successful in the reconstruction of space-time beams carrying small values of OAM [11, 24], the large OAM content associated with the structured beams using our broadband light source forces a relatively large off-axis angle to separate the first order interference terms. This results in a tilt between the pulse fronts of the interfering beams and an interference strip that drifts with the time delay out of the spatial region of interest [39], ultimately preventing the characterization of the complex beam evolution in space and time (Supplementary Note 6).

To overcome this obstacle, we introduce a hyperspectral holography technique (Fig. 2a) combining off-axis digital holography at a fixed delay of the reference with Fourier transform spectroscopy based on a common-path birefringent interferometer [28]—known as the Translating-Wedge-based Identical pulses eNcoding System (TWINS) [40]. The complete 3D information of the field is obtained by scanning the 1D temporal delay τ of the pulse replicas generated by the TWINS interferometer while recording the 2D spatial pattern of the off-axis interference (Fig. 2a), resulting in a temporal interferogram for every camera pixel (Fig. 2b). Then, by carrying out a temporal Fourier transform at every pixel we obtain a set of spectral images, whose spatial Fourier transform provides the amplitude and phase of the field, as in off-axis digital holography (Fig. 2c). The measurement is hyperspectral as it gives access to a continuous spectrum of images, rather than a discrete one as in multispectral imaging based on spectral filters. The outcome of this technique is the so-called spectral hypercube [41] providing the 3D data set of the complex field in space-frequency $\hat{E}(x,y,\omega)$ (rather than $E(x,y,t)$ in space-time, as in previous works using only off-axis holography). As in other techniques based on digital holography [42], the absolute spectral phase of the reference pulse needs to be characterized by an independent method, such as frequency-resolved optical gating, on the input NOPA pulse (Supplementary Note 4). Finally, by an inverse temporal Fourier transform we obtain $E(x,y,t)$ that, being fully characterized, can be propagated to any distance z. We note that a frequency-resolved characterization of space-time beams was also carried out in a previous work [13], by combining off-axis holography with spectrum scanning based on the

rotation of a spectral filter, though such approach can become challenging for broadband pulses like the ones implemented here.

The spatio-spectral phase reconstructed for a helical wave packet with hyperspectral holography shows that frequencies with different OAM correspond to circular beams with different diameters (Fig. 2d). This spatial chirp has a nontrivial influence on the local pulse duration of the helical wave packet, in particular when spectral chirp is also present, due to space-time coupling effects (see Supplementary Note 5 for an analysis). After carrying out a decomposition of the field on the OAM eigenstates [43] (Materials and Methods), we obtain the experimental signature of the topological-spectral correlation—a linear distribution of topological charges between $\ell = 30$ and 50—in excellent agreement with our design (Fig. 2e). The reconstructed helical wave packet is observed to rotate in space-time (Fig. 2f), in striking contrast to the position-independent dynamics of a separable pulsed vortex (Fig. 2g) despite the two beams carrying the same mean topological charge $\bar{\ell} = 40$ (see Supplementary Movies for animations and volumetric visualizations).

Linear topological-spectral correlations

Our broadband control of topological-spectral correlations makes it possible to verify—and, most importantly, to tailor to specific applications—many spatiotemporal properties of these light fields, which were predicted by a number of theories [17, 37, 44, 45] but not yet experimentally demonstrated, as we show in the following.

By changing the offset of the linear correlation, we can adjust the orbital radius of the rotating pulse. In Fig. 3a this radius is 48% larger than that of the beam shown in Fig. 2f—a scaling in agreement with the change in the mean topological charge, from 40 to 60. The chirality of the helical wave packet—namely, the sense of rotation of its intensity envelope—is controlled by the sign of the linear slope defining the correlations, rather than by that of the topological charges carried by the beam. By changing from a positive to a negative slope, one can observe in the y–t projection of Fig. 3b that the helix rotates in the opposite direction with respect to the beam of Fig. 3a (see also Extended Data Fig. 3a,b from the analytical theory derived in the Supplementary Note 7). The change of slope sign also corresponds to a reversal of the chromatic order of the concentric rings constituting the wave packet, as observed in the spectrally-resolved images obtained from the hyperspectral camera (Fig. 3a,b), emphasizing that our spatiotemporal beam shaping is an advanced form of spatial chirp engineering.

Multiple intertwined helices can be synthesized by changing the step size in the topological-spectral correlation (Extended Data Fig. 3b–d). For the case of $\delta\ell = 2$ and for the same OAM bandwidth of Fig. 3a, we observe the appearance of a second helix rotating in the same

direction (Fig. 3c). In this case we can clearly resolve the spectral windows, as their width (13.4 THz) is larger than the spectral resolution of the TWINS interferometer (7.9 THz). Finally, we show that we can combine all the previous types of control by multiplexing different correlations over the large topological and spectral bandwidths available in our system. To this end, in Fig. 3d, we synthesize two helices with different orbital radii and opposite chiralities, exploiting the low-frequency (red) spectral band to sweep charges from $\ell = 80$ to 70, and the high-frequency (green) one to go from $\ell = 40$ to 50.

Complex topological-spectral correlations

Our method of space-time beam shaping allows us to synthesize wave packets with arbitrary topological-spectral correlations, beyond the linear ones illustrated so far. We present in Fig. 4a,b two different kinds of complex correlations, corresponding to a square root and a parabolic function. (Additional linear and complex correlations synthesized experimentally are presented in Extended Data Fig. 2.) In each case we observe an excellent agreement between the design and the reconstructed experimental correlation.

In the case of the square root correlation, our simulations show that this produces a spatiotemporal behavior very similar to that of a helical wave packet synthesized from a linear correlation, but the rotating pulse has a larger angular velocity Ω (Extended Data Fig. 4). More generally, the orbital period of the pulse, $T_{\mathrm{orb}} = 2\pi/\Omega$, measured at a given z-plane (a.k.a. the temporal pitch of the helical wave packet) can be controlled by the exponent p of the power function appearing in the following complex correlation

$$\ell(\omega) = \left[\Delta\ell \left(\frac{\omega_2 - \omega}{\Delta\omega} \right)^p + \ell_1 \right], \tag{1}$$

where $\Delta\ell$ and $\Delta\omega$ are the OAM and spectral bandwidths, ℓ_1 and ω_2 are the lowest topological charge and the highest angular frequency of the correlation, and the square brackets indicate rounding to the nearest integer. As p becomes either smaller or larger than unity, the temporal pitch of the helical wave packet decreases (Fig. 4c, left), and in the limit $p \to 0$ or ∞ the space-time beam becomes a simple pulsed vortex with T_{orb} tending to zero (Fig. 4c, right).

For the parabolic correlation (Fig. 4b), we can understand the space-time dynamics of the beam by decomposing the function into two half-parabolas and studying them separately. We simulate each contribution by considering only half of the intensity spectrum. The two components correspond to power functions with $p = 2$ and opposite orientation, leading to helical wave packets with opposite chirality (Fig. 4d, left). The interference of the two counter-propagating pulses results into an achiral wave packet (Fig. 4d, right), with an iso-surface

structure very similar to the one observed experimentally. More generally, the chirality of a wave packet can be calculated using the following integral

$$\chi = \mathrm{sgn}\left(\int \frac{d\ell(\omega)}{d\omega} \, I(\omega)d\omega \right) \tag{2}$$

where $\ell(\omega)$ is the function relating OAM to frequency, and $I(\omega)$ is the intensity spectrum of the pulse. It can be seen that the integral vanishes for a parabolic correlation—as long as $I(\omega)$ and the parabola share the same axis of symmetry—thus $\chi = 0$, corresponding to an achiral wave packet.

Discussion

We have experimentally demonstrated a method for the spatiotemporal synthesis of ultrashort wave packets with broadband spectral and topological control. The wide range of topological charges opens the door to an entire new family of OAM-carrying space-time beams with many properties yet to be explored. In addition to OAM, other degrees of freedom of light could be spectrally tailored in our setup, including the spectral intensities via amplitude modulation and the relative phases among the different spatiospectral modes of the pulse, while polarization could be controlled by replacing the modulator with a metasurface [18]. Moreover, by adding an amplitude mask the system could be changed from the generation of Bessel beams to Mathieu [46] or parabolic [47] beams, resulting into pulses with elliptical or parabolic profiles, rather than circular. Our hyperspectral holographic characterization technique is ideally suited for the spatiotemporal metrology of these broadband beams, since it does not require an iterative algorithm as in other spatially-resolved spectral techniques [48–51]. Our method can resolve temporal features shorter than the duration of the reference pulse, in contrast to approaches based on temporal cross-correlation scanning the delay between the structured and reference beam. Moreover, hyperspectral holography could be easily extended in the future to reconstruct also the polarization distribution of vectorial space-time wave packets [18, 23, 52, 53]. The space-time beams generated with the technique presented here could soon find use in transferring OAM to matter, such as in Raman processes (stimulated Raman scattering) at the core of laser-plasma accelerators [54], in the imaging of ultrafast charge carrier diffusion processes thanks to the mapping of time to space carried out by helical wave packets, and in increasing the capacity of optical communication channels thanks to OAM-frequency division multiplexing [55].

Acknowledgements

Author contribution

M.P. conceived the original idea. M.P., M.O., V.R.P., M.R., G.V., C.M., G.C., A.A. designed the experiments. M.P., M.O., V.R.P., M.R., B.A., M.C. performed the measurements. M.P., J.V. performed the theory and simulations. M.P., M.O. fabricated the devices. M.P., V.R.P., B.A., M.C., C.M. analyzed the experimental data. All authors contributed to the interpretation of results and to the writing of the manuscript.

Competing interests

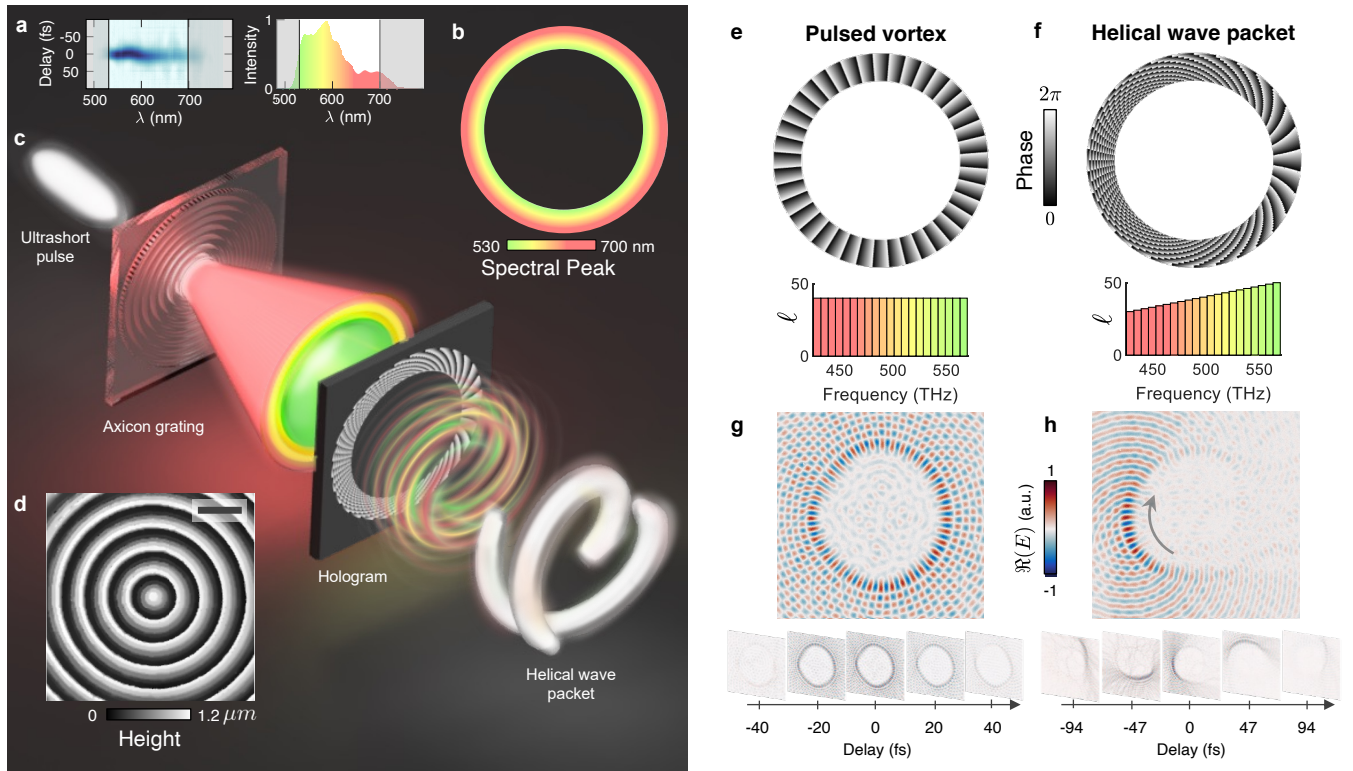The authors declare that they have no competing interests.

Figures

Fig. 1. **Synthesizing space-time beams with broadband topological-spectral correlations. a**, Characterization trace of the femtosecond pulses from the non-collinear optical parametric amplifier measured by polarization-gated frequency-resolved optical gating (FROG, left). The intensity spectrum covers a broad portion of the visible range (right). The gray shaded areas mask the unused part of the spectrum, where the root mean square noise is above 0.5% of the signal. **b**, Spectral peak distribution in the far field of the axicon characterized by an hyperspectral camera. **c**, Conceptual scheme for space-time beam shaping, with an axicon grating mapping the spectral content of the input ultrashort pulse into concentric rings. A hologram displayed on a spatial light modulator in the far field of the axicon tailors a topological-spectral correlation, resulting in helical wave packets. For clarity, the beam path is shown along a straight line here, whereas in the setup it is folded (Fig. 2a). **d**, Optical profilometry image of the fabricated grayscale axicon. Scale bar is 50 μm. **e**, Hologram used to generate a pulsed vortex with a topological charge $\ell = 40$ at all frequencies. **f**, Hologram used for the synthesis of a helical wave packet with a broadband linear topological-spectral correlation between $\ell = 30$ and 50. **g,h**, Real part of the electric field of the pulsed vortex and helical wave packet, respectively, obtained by on-axis holography. Image size in **g,h** is 2.5 mm × 2.5 mm; the largest plots are at a delay of 0 fs. Red-to-green colors in **a,b,e,f** directly correspond to the visible wavelengths/frequencies.

* marco.piccardo@inesc-mn.pt

† antonio.ambrosio@iit.it

[1] Jolly, S. W., Gobert, O. & Quéré, F. Spatio-temporal characterization of ultrashort laser beams: a tutorial. *Journal of Optics* **22**, 103501 (2020).

[2] Forbes, A., de Oliveira, M. & Dennis, M. R. Structured light. *Nature Photonics* **15**, 253–262 (2021).

[3] Divitt, S., Zhu, W., Zhang, C., Lezec, H. J. & Agrawal, A. Ultrafast optical pulse shaping using dielectric metasurfaces. *Science* **364**, 890–894 (2019).

[4] Shen, Y. *et al.* Roadmap on spatiotemporal light fields. *Preprint at https://arxiv.org/abs/2210.11273* (2022).

[5] Yessenov, M., Hall, L. A., Schepler, K. L. & Abouraddy, A. F. Space-time wave packets. *Adv. Opt. Photon.* **14**, 455–570 (2022).

[6] Piccardo, M. *et al.* Roadmap on multimode light shaping. *Journal of Optics* **24**, 013001 (2022).

[7] He, C., Shen, Y. & Forbes, A. Towards higher-dimensional structured light. *Light: Science & Applications* **11**, 205 (2022).

[8] Wright, L. G., Wu, F. O., Christodoulides, D. N. & Wise, F. W. Physics of highly multimode nonlinear optical systems.
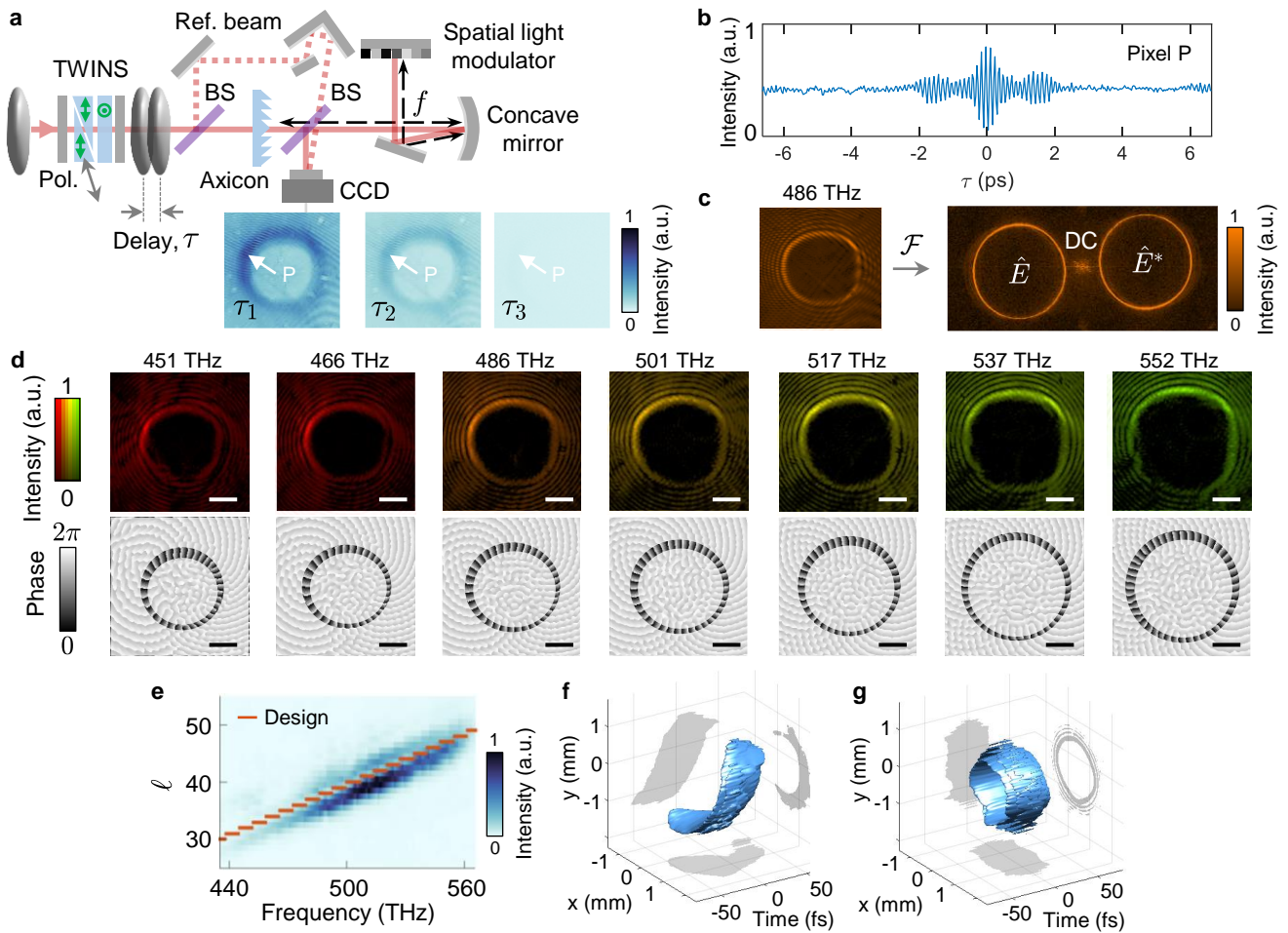
Fig. 2. **Spatiotemporal characterization based on hyperspectral off-axis holography. a**, Schematic of the spatially-resolved spectral setup introduced for the space-time beam characterization. It combines a spatial interferometer based on off-axis digital holography with a temporal one based on Fourier transform spectroscopy using a common-path birefringent interferometer, the Translating-Wedge-based Identical pulses eNcoding System (TWINS). Both the axicon and the SLM lie at the focal distance (f) of the concave mirror. Three images recorded by the CCD camera, which lies at the image plane ($4f$) of the axicon, show the change in signal intensity at different delays τ of the TWINS interferometer, ranging from constructive (τ_1) to destructive interference (τ_3). BS, beamsplitter. **b**, Interferogram signal at the pixel P marked in **a**. **c**, Off-axis interference image at 486 THz that, upon a digital spatial Fourier transform, gives the first-order complex conjugates of the electric field ($\hat{E}$ and $\hat{E}^*$) and the non-interfering components (DC). **d**, Intensity and phase images of the complex electric field obtained after the off-axis digital holography analysis and shown for a selected set of frequencies from the hyperspectral cube. The scale bars are 500 μm. **e**, Experimental topological-spectral correlation of a helical wave packet obtained by modal decomposition. **f,g**, Iso-intensity surfaces at 10% of the intensity peak for the helical wave packet with the correlation shown in **e** and for a pulsed vortex with constant $\bar{\ell} = 40$. The qualitative features of the iso-surfaces are independent from the specific percentage level chosen for the cut.

Nature Physics **18**, 1018–1030 (2022).

[9] Kondakci, H. E. & Abouraddy, A. F. Diffraction-free space-time light sheets. *Nature Photonics* **11**, 733–740 (2017).

[10] Bhaduri, B., Yessenov, M. & Abouraddy, A. F. Anomalous refraction of optical spacetime wave packets. *Nature Photonics* **14**, 416–421 (2020).

[11] Yessenov, M. *et al.* Space-time wave packets localized in all dimensions. *Nature Communications* **13**, 4573 (2022).

[12] Rego, L. *et al.* Generation of extreme-ultraviolet beams with time-varying orbital angular momentum. *Science* **364**, eaaw9486 (2019).

[13] Cruz-Delgado, D. *et al.* Synthesis of ultrafast wavepackets with tailored spatiotemporal properties. *Nature Photonics* **16**, 686–691 (2022).

[14] Chong, A., Wan, C., Chen, J. & Zhan, Q. Generation of spatiotemporal optical vortices with controllable transverse orbital angular momentum. *Nature Photonics* **14**, 350–354 (2020).

[15] Wang, H., Guo, C., Jin, W., Song, A. Y. & Fan, S. Engineering arbitrarily oriented spatiotemporal optical vortices using
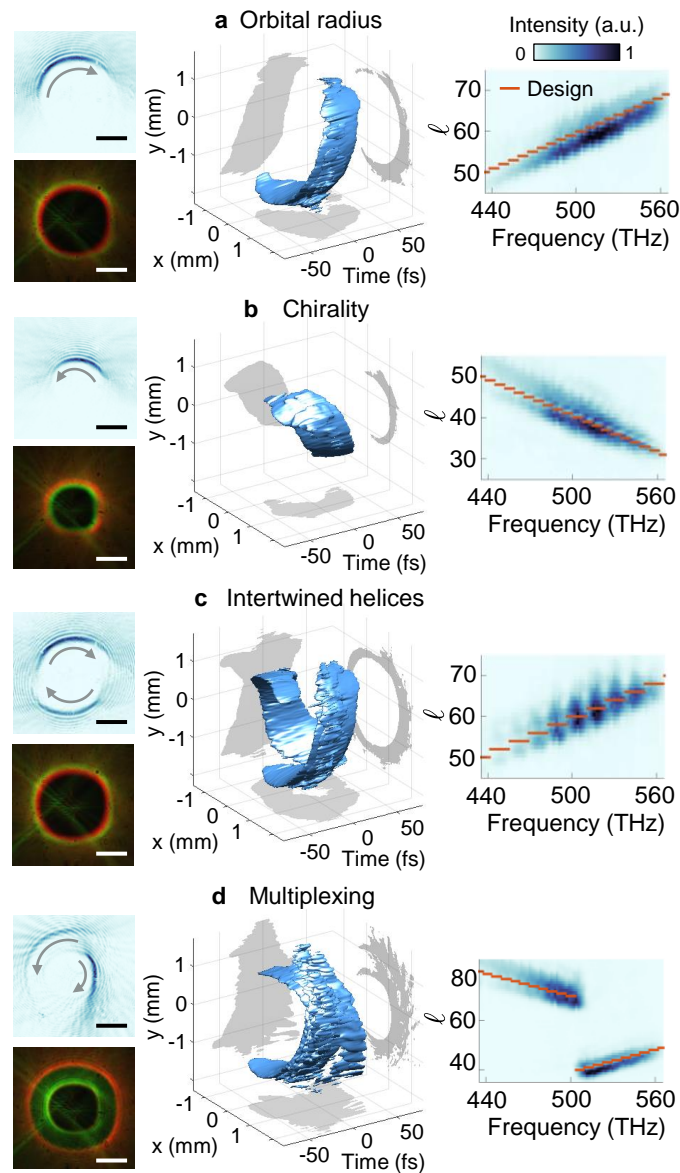
Fig. 3. **Controlling helical wave packets by tailoring linear correlations.** The synthesis of arbitrary linear topological-spectral correlations allows us to precisely control different properties of helical wave packets: **a**, the orbital radius of the rotating intensity envelope; **b**, the direction of rotation; **c**, the number of intertwined helices; **d**, multiplexing different helices with a combination of the previous properties using different spectral bands. Each panel shows the intensity of the electric field at $t = 0$ (top left), the time-averaged color image of the beam obtained by an hyperspectral camera (bottom left), the iso-surface at 10% of the intensity peak (center), and the experimental correlation (right). The scale bars are 1 mm. Animations and volumetric visualization are shown in Supplementary Movies.

transmission nodal lines. *Optica* **8**, 966–971 (2021).

[16] Chen, W. *et al.* Time diffraction-free transverse orbital angular momentum beams. *Nature Communications* **13**, 4021 (2022).

[17] Pariente, G. & Quéré, F. Spatio-temporal light springs: extended encoding of orbital angular momentum in ultrashort pulses. *Opt. Lett.* **40**, 2037–2040 (2015).

[18] Chen, L. *et al.* Synthesizing ultrafast optical pulses with arbitrary spatiotemporal control. *Science Advances* **8**, eabq8314 (2022).

[19] Zhao, Z. *et al.* Dynamic spatiotemporal beams that combine two independent and controllable orbital-angular-momenta using multiple optical-frequency-comb lines. *Nature Communications* **11**, 4099 (2020).

[20] Zdagkas, A. *et al.* Observation of toroidal pulses of light. *Nature Photonics* **16**, 523–528 (2022).

[21] Wan, C., Cao, Q., Chen, J., Chong, A. & Zhan, Q. Toroidal vortices of light. *Nature Photonics* **16**, 519–522 (2022).
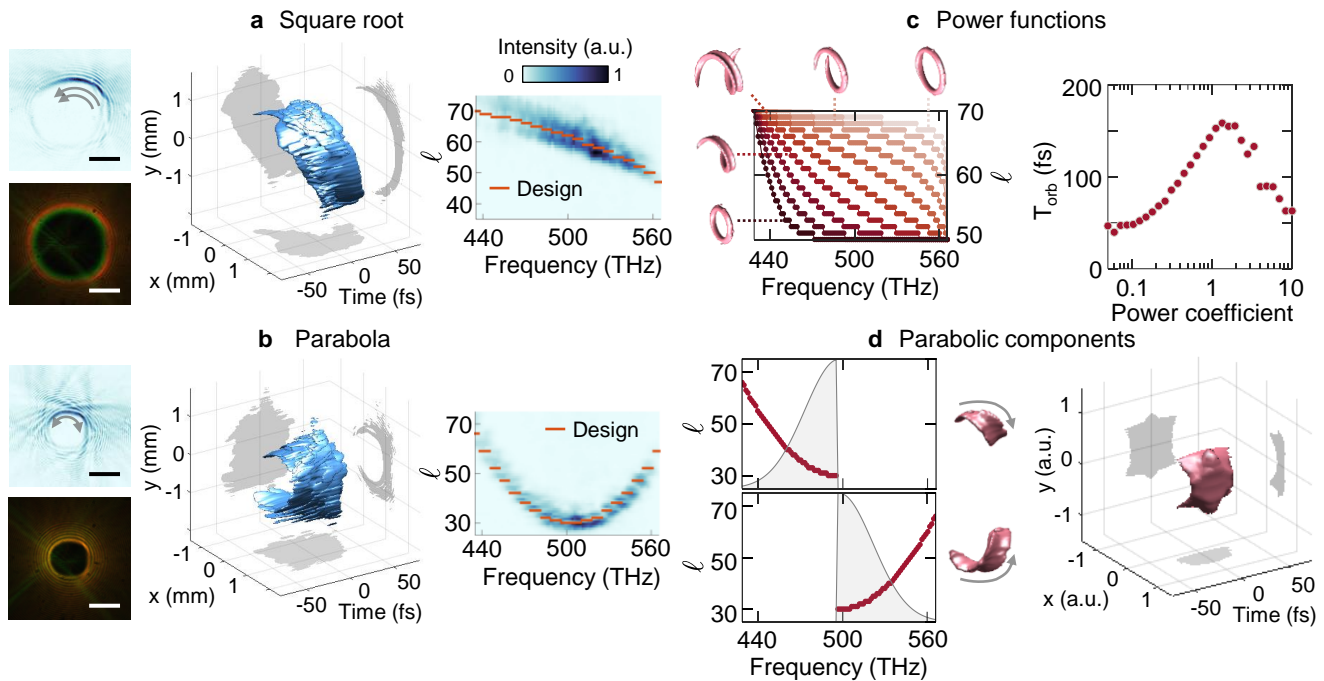
Fig. 4. **Complex topological-spectral correlations.** Synthesis of OAM-carrying space-time beams with different correlations beyond linear: **a**, square root function, and **b**, parabolic function. Each panel shows the intensity of the electric field at $t = 0$ (top left), the time-averaged color image of the beam obtained by an hyperspectral camera (bottom left), the iso-surface at 10% of the intensity peak (center), and the experimental correlation (right). The scale bars are 1 mm. **c**, Family of complex correlations described by the power function of equation 1 for different values of p logarithmically spaced from 0.07 (top, light orange) to 10 (bottom, dark red). Simulated iso-surfaces of the space-time beams are shown for p equal to: 0.07, 0.21, 1.12, 2.32, 10. Also shown is the orbital period (T_{orb}) of the rotating pulse as a function of p (right). **d**, Simulation of the left and half components of a parabolic correlation function (left). The shaded area corresponds to the normalized intensity spectrum. The simulations give helical wave packets with opposite chirality. The right plot shows the simulated isosurface when considering the entire parabolic correlation function. Animations and volumetric visualization are shown in Supplementary Movies.

[22] Wang, J. *et al.* Terabit free-space data transmission employing orbital angular momentum multiplexing. *Nature Photonics* **6**, 488–496 (2012).

[23] Mounaix, M. *et al.* Time reversed optical waves by arbitrary vector spatiotemporal field generation. *Nature Communications* **11**, 5813 (2020).

[24] Zou, K. *et al.* Tunability of space-time wave packet carrying tunable and dynamically changing OAM value. *Opt. Lett.* **47**, 5751–5754 (2022).

[25] Cerullo, G. & De Silvestri, S. Ultrafast optical parametric amplifiers. *Review of Scientific Instruments* **74**, 1–18 (2003).

[26] Manzoni, C. & Cerullo, G. Design criteria for ultrafast optical parametric amplifiers. *Journal of Optics* **18**, 103501 (2016).

[27] Zavelani-Rossi, M. *et al.* Pulse compression over a 170-THz bandwidth in the visible by use of only chirped mirrors. *Opt. Lett.* **26**, 1155–1157 (2001).

[28] Perri, A. *et al.* Hyperspectral imaging with a TWINS birefringent interferometer. *Opt. Express* **27**, 15956–15967 (2019).

[29] McGloin, D. & Dholakia, K. Bessel beams: Diffraction in a new light. *Contemporary Physics* **46**, 15–28 (2005).

[30] Dardikman, G. & Shaked, N. T. Is multiplexed off-axis holography for quantitative phase imaging more spatial bandwidth-efficient than on-axis holography? [invited]. *J. Opt. Soc. Am. A* **36**, A1–A11 (2019).

[31] Tokizane, Y., Oka, K. & Morita, R. Supercontinuum optical vortex pulse generation without spatial or topological-charge dispersion. *Opt. Express* **17**, 14517–14525 (2009).

[32] Bouchard, F., Mand, H., Mirhosseini, M., Karimi, E. & Boyd, R. W. Achromatic orbital angular momentum generator. *New Journal of Physics* **16**, 123006 (2014).

[33] Wakayama, T. *et al.* Generation of achromatic, uniform-phase, radially polarized beams. *Opt. Express* **22**, 3306–3315 (2014).

[34] Radwell, N., Hawley, R. D., Götte, J. B. & Franke-Arnold, S. Achromatic vector vortex beams from a glass cone. *Nature Communications* **7**, 10564 (2016).

[35] Naik, D. N., Saad, N. A., Rao, D. N. & Viswanathan, N. K. Ultrashort vortex from a gaussian pulse - an achromatic-interferometric approach. *Scientific Reports* **7**, 2395 (2017).

[36] Berry, M. V. Optical vortices evolving from helicoidal integer and fractional phase steps. *Journal of Optics A: Pure and Applied Optics* **6**, 259 (2004).

[37] Porras, M. A. Attosecond helical pulses. *PRA* **100**, 033826 (2019).

[38] Cuche, E., Bevilacqua, F. & Depeursinge, C. Digital holography for quantitative phase-contrast imaging. *Opt. Lett.* **24**, 291–293 (1999).

[39] Maznev, A. A., Crimmins, T. F. & Nelson, K. A. How to make femtosecond pulses overlap. *Opt. Lett.* **23**, 1378–1380 (1998).

[40] Brida, D., Manzoni, C. & Cerullo, G. Phase-locked pulses for two-dimensional spectroscopy by a birefringent delay line. *Opt. Lett.* **37**, 3027–3029 (2012).

[41] Genco, A. *et al.* k-space hyperspectral imaging by a birefringent common-path interferometer. *ACS Photonics* **9**, 3563–3572 (2022).

[42] Gabolde, P. & Trebino, R. Self-referenced measurement of the complete electric field of ultrashort pulses. *Opt. Express* **12**, 4423–4429 (2004).

[43] Pinnell, J. *et al.* Modal analysis of structured light with spatial light modulators: a practical tutorial. *J. Opt. Soc. Am. A* **37**, C146–C160 (2020).

[44] Béjot, P. & Kibler, B. Spatiotemporal helicon wavepackets. *ACS Photonics* **8**, 2345–2354 (2021).

[45] Béjot, P. & Kibler, B. Quadrics for structuring invariant space-time wavepackets. *ACS Photonics* **9**, 2066–2072 (2022).

[46] Gutiérrez-Vega, J. C., Iturbe-Castillo, M. & Chávez-Cerda, S. Alternative formulation for invariant optical fields: Mathieu beams. *Opt. Lett.* **25**, 1493–1495 (2000).

[47] Bandres, M. A. Accelerating parabolic beams. *Opt. Lett.* **33**, 1678–1680 (2008).

[48] Miranda, M. *et al.* Spatiotemporal characterization of ultrashort laser pulses using spatially resolved fourier transform spectrometry. *Opt. Lett.* **39**, 5142–5145 (2014).

[49] Pariente, G., Gallet, V., Borot, A., Gobert, O. & Quéré, F. Space-time characterization of ultra-intense femtosecond laser beams. *Nature Photonics* **10**, 547–553 (2016).

[50] Borot, A. & Quéré, F. Spatio-spectral metrology at focus of ultrashort lasers: a phase-retrieval approach. *Opt. Express* **26**, 26444–26461 (2018).

[51] Jolly, S. W., Gobert, O. & Quéré, F. Spatio-spectral characterization of ultrashort laser pulses with a birefringent delay line. *OSA Continuum* **4**, 2044–2051 (2021).

[52] Alonso, B. *et al.* Complete spatiotemporal and polarization characterization of ultrafast vector beams. *Communications Physics* **3**, 151 (2020).

[53] Yessenov, M., Chen, Z., Lavery, M. P. J. & Abouraddy, A. F. Vector space-time wave packets. *Opt. Lett.* **47**, 4131–4134 (2022).

[54] Vieira, J., Mendonça, J. T. & Quéré, F. Optical control of the topology of laser-plasma accelerators. *PRL* **121**, 054801 (2018).

[55] Willner, A. E. *et al.* Perspectives on advances in high-capacity, free-space communications using multiplexing of orbital-angular-momentum beams. *APL Photonics* **6**, 030901 (2021).

Materials and Methods

Multilevel axicon grating fabrication

We fabricate the axicon as a grayscale phase mask on a 500 μm thick fused silica substrate. Prior to the fabrication of the axicon, we perform a grayscale dose matrix to calibrate the dose and defocus of the laser writer. We perform the grayscale lithography by exposing five layers (each corresponding to a set of concentric axicon rings at different height levels) in sequence. The fabrication process consists in spin-coating a primer (TI Prime: 6000 rpm, 500 rpm/s, 60 s, bake 2 min at 120°C), followed by a positive photoresist (AZ5214: 4000 rpm, 500 rpm/s, 60 s, bake 90 s at 110°C), then direct laser writing (Heidelberg MLA100), development (AZ726: 60 s), reactive ion etching (50 sccm CHF$_3$, 5 sccm O$_2$ etch: 100 W RF, 500 W inductively coupled plasma, 5 Pa pressure), and resist dissolve (acetone bath).

Axicon design

The diameter of the fabricated axicon is $\varnothing = 10$ mm and the grating period is $d = 25$ μm to maximize the spectral resolution of the space-time synthesizer for a mirror focal length of $f = 150$ mm, while the axicon height of 1200 nm corresponds to a 2π phase shift for a wavelength of 552 nm ($n_{\mathrm{SiO}_2} = 1.46$), in the range of the NOPA. In the far field of the axicon, each spectral component of wavelength λ corresponds to an annular beam of radius $R = f\lambda/d$ and half-thickness $T = f\lambda/\pi w_0$ [56], where $w_0 = 2.16$ mm is the input beam waist. The spectral resolution of the grating is given by $\delta\lambda = \lambda\, 2T/R$. We characterize the parameter $R/2T = \pi w_0/2d = 136$ of our system by shining a nearly monochromatic HeNe source on the axicon, obtaining that $\delta\lambda$ lies in the range between 4 and 5 nm over the pulse bandwidth. From the relationship between the spectral bandwidth, $\Delta\lambda$, and the average spectral resolution, $\delta\lambda$, we calculate that our system can address around 40 independent spectral windows. This number can be increased either by enlarging the input beam waist and axicon diameter or by reducing the grating period. To avoid the annular beam diameter becoming larger than the SLM size in the latter case one can reduce f, which also makes the system more compact. Finally, taking a typical annular beam radius of 4 mm in our system, the SLM pixel size $d_{\mathrm{SLM}} = 8$ μm, and

requiring at least 8 pixels per azimuthal sector (spanning a phase ramp from 0 to 2π), we estimate that the largest topological charge that can be imparted in our scheme is around $\ell = 2\pi R/8d_{\mathrm{SLM}} \approx 400$.

Non-collinear optical parametric amplifier

The light source is obtained by pumping a non-collinear optical parametric amplifier (NOPA) [26] with a Ti:Sapphire laser that emits 100 fs pulses peaked at 800 nm with a repetition rate of 1 kHz. The pulse duration of the compressed NOPA was estimated to be 7 fs based on PG FROG characterization with an added 3.4 mm of fused silica glass in the beam path, which introduces a similar amount of positive GVD as the structured light setup optics (Supplementary Note 4, Sec. A). The NOPA spectrum spans from approximately 520 nm to 730 nm. Given the high sensitivity of the holography techniques to spectral noise, we filter out the edges of the base NOPA spectrum, which have the highest RMS noise, resulting in a spectrum with an RMS below 0.5%. In particular, the longer wavelength portion of the spectrum shows higher noise due to its proximity to the laser fundamental at 800 nm but also due to limitations of the chirped mirrors used for pulse compression at longer wavelengths. The output of the NOPA is sent through a first reflective telescope with two concave mirrors (75 mm and 250 mm focal length) and a pinhole ($\varnothing = 100~\mu$m) used to filter the beam and reduce its spatial chirp [57] (Fig. S6), and then through a second telescope with a magnification factor $3\times$ to increase the Gaussian beam diameter to approximately 10 mm, matching the diameter of the axicon.

Space-time beam shaper

The NOPA beam is fed into the space-time beam shaper following a broadband half-wave plate to set the polarization along the modulation axis of the spatial light modulator (SLM). We use broadband UV fused silica beamsplitters (BSW10R, 1 mm thick) for the realization of the interferometer for the holographic measurements. The focal length of the concave mirror used for the spatial Fourier transform is 150 mm. The SLM is a phase-only liquid crystal modulator (Holoeye PLUTO-2.1-NIR-133 broadband module). The holograms displayed on the SLM impart, in addition to the desired topological-spectral correlation, astigmatic aberration corrections that are implemented via Zernike polynomials. We convert the target phase profile into a matrix of SLM voltage levels that accounts for the wavelength-dependent response of the modulator, exploiting the fact that the wavelengths constituting the broadband pulse are spatially dispersed at the SLM plane. We block the zero order of the axicon, corresponding to a focused spot in the far field, by placing a mask with a metallic disk ($\varnothing = 2$ mm) just in front of the SLM (not shown in Fig. 2a). The delay line for the reference path uses a hollow rooftop mirror on a motorized micrometer stage. The output of the spatiotemporal synthesizer is magnified by a factor $5\times$ using concave mirrors, to increase the size of the fringes used in the holographic characterization. We add a small propagation distance (of the order of a few cm) from the image plane of the axicon before detection to allow the formation of the Bessel beam, due to coupling between the phase and amplitude of the beam along propagation. We use high resolution CCD cameras for the beam characterization (LT665 Spiricon for on-axis holography, and PointGrey GS3-U3-23S6M).

Hyperspectral off-axis holography

The spatiotemporal characterization technique we introduce relies on two interferometers, a temporal one based on the common-path birefringent interferometer [40] and a spatial one based on off-axis holography. The TWINS interferometer consists of a set of two birefringent alpha barium borate (α-BBO) wedges ($7°$ apex angle) followed by an α-BBO plate. The wedges and the plate have crossed optical axes, and the setup is sandwiched between two linear polarizers (Fig. 2a). TWINS generates two replicas of the input waveform whose delay can be controlled by varying the insertion of one of the wedges. The length of the delay scan is 4 mm in steps of 10 μm and, combined with our interferogram apodization (Happ-Genzel), gives a spectral resolution of 7.9 THz. The spatial component of the interferometer relies on interfering the space-time beam with a reference (the pulsed Gaussian beam prior to shaping) at a small angle. This angle is adjusted by making sure that the rings corresponding to the complex conjugate Fourier transform of the electric field, $\hat{E}$ and $\hat{E}^*$, do not overlap (Fig. 2c). We set the delay zero of the spatial interferometer by finding the condition in which the spatial fringes are centered with respect to the position of the time-averaged intensity image of the space-time beam (note that these fringes drift as a function of the delay between the shaped and reference beam), then we do not modify this delay over the measurement. This consists in acquiring an interference image (20 ms integration time) for every temporal delay of the TWINS interferometer. We also carry out a background measurement in absence of the reference beam (thus without any spatial interference), which is subtracted from the previous set of data to reduce the DC contribution in the digital Fourier transform (Fig. 2c). The data processing provides the hyperspectral cube, consisting of spectrally-resolved images of off-axis interference. On each image we apply the procedure of off-axis digital holography by isolating only one of the complex conjugates of the reciprocal electric field, and then by inverse Fourier transform we obtain a new hyperspectral cube giving a set of spectral images of the amplitude and phase of the complex electric field constituting the synthesized space-time beam. Importantly,

due to the angle used for off-axis interference, the temporal overlap between the structured and the reference beams occurs only along a spatial strip whose position is delay dependent. We correct for this by developing a procedure to digitally remove the tilt between the pulse front of the reference and structured beam (Supplementary Note 6).

Topological-spectral correlations

The experimental topological-spectral correlations are obtained by carrying out a modal decomposition of each spectral image on the OAM eigenstates [43]. These are phase-only functions with no amplitude components, which do not constitute a true (i.e. orthonormal) basis but can be used to determine the OAM content of an optical field, therefore we used them to compare experimentally the topological-spectral correlations with the design curves used to configure the SLM. The spectral accuracy in the absolute position of the correlation points is estimated to 5 THz, given by a combination of the TWINS accuracy (> 1 THz) and an uncertainty in experimentally matching the position of the SLM hologram with respect to the radial distribution of wavelengths in the far field of the axicon. While carrying out the overlap integral and projecting to the far field for the modal decomposition, we observe that the different frequencies have a slightly different angle: for the reference case of a pulsed vortex, where $\ell = 40$ for any ω, a small shift of the spot is seen in the far field. We account for this shift and establish a calibration based on the pulsed vortex beam, which is then applied to the modal decomposition of all space-time beams studied in this work. The non-uniformity in the spectral rings of Fig. 2d is attributed to a small amount of residual spatial chirp in the input NOPA pulse [57], which we characterized with a spectrally-resolved beam profiler (Extended Data Fig. 5).

Numerical simulations

Simulations are carried out by calculating the interference of Bessel-Gauss beams with different spectral frequency and topological charge, as determined by a given correlation function. We consider 100 modes spanning the same frequency range of the NOPA pulse used in the experiments. Unless otherwise stated, we assume a flat spectral phase for the input pulse.

Data availability

The datasets generated during the current study are available from the corresponding author on reasonable request.

---

[*] marco.piccardo@inesc-mn.pt

[†] antonio.ambrosio@iit.it

[56] Pinnell, J., Rodríguez-Fajardo, V. & Forbes, A. How perfect are perfect vortex beams? *Opt. Lett.* **44**, 5614–5617 (2019).

[57] Harth, A. *et al.* Compact 200 kHz HHG source driven by a few-cycle OPCPA. *Journal of Optics* **20**, 014007 (2018).